AIP | Review of Scientific Instruments

Image time-correlation, dynamic light scattering, and birefringence for the study of the response of anisometric colloids to external fields

Kyongok Kang

Citation: Rev. Sci. Instrum. **82**, 053903 (2011); doi: 10.1063/1.3589856
View online: http://dx.doi.org/10.1063/1.3589856
View Table of Contents: http://rsi.aip.org/resource/1/RSINAK/v82/i5
Published by the American Institute of Physics.

REVIEW OF SCIENTIFIC INSTRUMENTS **82**, 053903 (2011)

Image time-correlation, dynamic light scattering, and birefringence for the study of the response of anisometric colloids to external fields

Kyongok Kang
Forschungszentrum Jülich, ICS-3, Soft Condensed Matter, D-52425 Jülich, Germany

(Received 2 November 2010; accepted 19 April 2011; published online 18 May 2011)

In this paper, a detailed description of equipment is given, specially designed to characterize the response of non-spherical colloids to external fields. To characterize slow structural changes on a large length scale we developed an image correlation method, fast dynamics on the colloidal-particle level is probed by means of a vertically mounted, small angle dynamic light scattering setup, while the orientational order (induced by the external field) is measured with a birefringence setup with off-normal incidence. The performance of this *in situ* set of instruments is illustrated by experiments on concentrated dispersions of very long and thin, charged colloidal rods (fd-virus particles) in external electric fields. Here, the frequency of the field is sufficiently low to polarize electrical double layers, leading to additional inter-colloidal interactions which are found to give rise to phase/state transitions and dynamical states (K. Kang and J. K. G. Dhont, Soft Matter **6**, 273, 2010). © *2011 American Institute of Physics*. [doi:10.1063/1.3589856]

I. INTRODUCTION

There is an increasing interest in the response of suspensions to external fields, particularly in an electric fields,[1–6] which can be used to induce and direct self-assembly of charged colloids (see Ref. 7 for a detailed overview as well as Ref. 8 where also other types of external fields are discussed). Such phenomena are of interest from a fundamental point of view and can sometimes be employed for practical purposes. In order to gain in the understanding of these complicated phenomena, we developed an *in situ* set of instruments to probe the bulk phase behavior of charged colloidal rods and their interactions under an externally applied electric field. We recently reported on the response of charged colloidal rods to an alternating electric field,[9,10] where it was found that different stationary phases/states and dynamical states can be induced, depending on the field amplitude and frequency. These phases/states and dynamical states are the result of inter-particle interactions that are due to polarization of the particle's double layers as well as electro-osmotic flow. We observed a transition from non-chiral nematic to chiral nematic, to dynamical states where nematic domains melt and reform at low frequencies, while at relatively high frequency a uniform homeotropically aligned state is found. So far there is no understanding of why these phases/states are formed, and the equipment described in this paper may contribute to resolve the mechanisms underlying such phenomena.

Time-correlation spectroscopy is a widely used method to obtain information about the dynamics of various types of systems and plays an important role in soft-matter research, such as in optical communication, biological imaging, and physical chemistry. With the advent of femtosecond lasers, optical studies of solvent dynamics and molecular dynamics of different solvents are now experimentally feasible, and in addition theory and simulations have been developed for a quantitative interpretation of the experimental results.[11–19] Typically, a time-gated stimulated photon echo (of a few hundred femtoseconds duration) requires a relatively high time resolution and high peak power to probe the fast dynamics of molecular motion in liquids.[20–22] To detect the microstructure inside a turbid or thick sample, a time-gated Raman amplifier can be used to detect structural images of dense scatterers (various sizes of polystyrene spheres).[23] However, it is still a challenge to probe the longer meanfree path of the scattered light in soft-matter or biological media, for instance in the case of tumors in soft tissue.[21,24] The reason for that is the lack of either transmitted laser power intensity or illumination time for a much longer meanfree path of the scattered light. Although in this case, diffusing wave spectroscopy is possible in principle, data interpretation is generally problematic. Thus the optimization of time-gated spectroscopy is necessary, depending on the particular system and purpose of the experiment. Especially the combination of both appropriate time domain and correlational length is left as an important task. In particular for soft-condensed matter systems, several experimental techniques are required to probe a broad variation of length and time scales.

In order to illustrate the performance of our set of instruments, we consider suspensions of charged fibrous viruses (fd-virus) as a model system for charged colloidal rods, in an external alternating electric field. Fd-virus is by now a standard model system for charged colloidal rods, the production of which is well established. Since the fd-virus particles are only slightly birefringent and their scattering strength is quite small as compared to other rod-like colloids, we expect the performance of our equipment to be at least as good for other types of colloidal-rod suspensions than fd-virus. Bacteriophage fd is a rod-like macromolecule with a length of $L = 880$ nm, a bare diameter of $D = 6.6$ nm, a persistence length at high salt concentration of $P = 2200$ nm, and a molecular weight of $M = 1.64 \times 10^7$ g/mol.[25–27] The response of fd-virus suspensions to an electric field has been shown to be dependent on the ionic strength.[27–29] In this paper, we use suspensions of fd-virus particles at a low ionic strength to ensure thick electric double layers. Slow dynamics within dynamical states on a large length scale are characterized by means of image time-correlation functions.[28,30] In addition, a small angle vertically aligned dynamic light scattering setup is used for microscopic dynamics under an electric field, and orientational order is probed by means of a vertically mounted birefringence setup with off-normal laser-beam incidence.

The instrumentation discussed in the present paper is developed for probing both the slow dynamics of large structures in dynamical states and the relatively fast microscopic dynamics on the colloidal-particle level, together with the determination of orientational order due to field-induced self-assembly. In addition to the optics, electronics, and software, a sample cell has been used that can be shared between the mentioned three setups. In Sec. II, a description of the instrumentation is given, while the performance of the instrumentation is discussed in Sec. III.

II. *IN SITU* ELECTRIC-FIELD INSTRUMENTS

An *in situ* electric cell is constructed that can be shared between all setups, i.e., the microscope that is used for image intensity time-correlation, the dynamic light scattering setup , and the birefringence setup. Figure 1 gives an overall view of the *in situ* electric field instruments, where the electrical-cell is encircled. We discuss each of the setups in this section. The sample cell will be described in Subsection A. Image intensity time-correlation spectroscopy is addressed in Subsection B, birefringence is discussed in Subsection C, and small angle dynamic light scattering in Subsection D. Note that all setups are vertically mounted due to the use of two flat indium-tin-oxide (ITO) electrodes that constitute the sample cell, which contains the suspension.

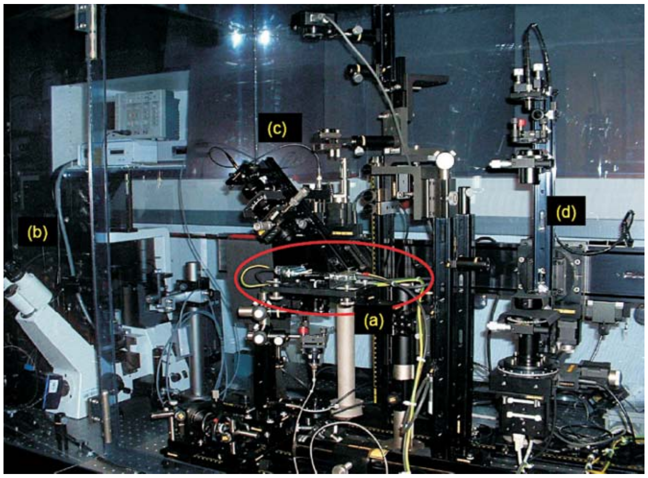

FIG. 1. (Color) An overview of the *in situ* electric-field instruments: (a) encircled, the optically transparent ITO electrical cell, (b) an inverted polarization microscope for image time-correlation spectroscopy, (c) the vertical dynamic light scattering setup, and (d) the electric birefringence setup. Each setup can be facilitated with the same electrical cell.

A. The *in situ* electrical cell

A homemade optically transparent electrical cell is used to facilitate imaging through a microscope, birefringence measurements, and dynamic light scattering experiments. We use commercially available custom-designed ITO coated float glass (from Präzisions Glas und Optik GmbH, CEC500S) of dimensions 40 × 70 mm^2 with a thickness of 0.7 mm. The ITO layer has a high visible light transmission (90%) at 633 nm and the coating thickness is 15 nm. Figure 2(a) shows a schematic side view of the *in situ* electric cell, where the sample is contained in between two ITO coated glass slides. The ITO coatings are electrically connected to a function generator (Avtech model AV-151G-B, 1 Hz−350 kHz, maximum ±200 V, load resistance $\geq$ 50 kΩ) via electronic pins (whose dimensions are 50 × 35 mm^2). Various types of waveforms and pulses can be applied by the function generator. In the experiments presented here, a sinusoidally varying electric potential is applied to the electrodes. The two glass slides are held apart by an insulating rectangular PTFE teflon ring film-spacer (Armbrecht and Matthes GmbH, AR5038 and AR5038GP), within which the sample is contained. Finally, teflon tape is used to fixate the glass slides together and to prevent sample evaporation. We always used 400 μl of sample, after which the precise distance between the electrodes is calculated from the radius of the circular sample. The sample is held into place through capillary forces and has a circular shape with a radius of about 20 mm. The typical distance between the electrodes is 1.40 ± 0.10 mm. Measurements are

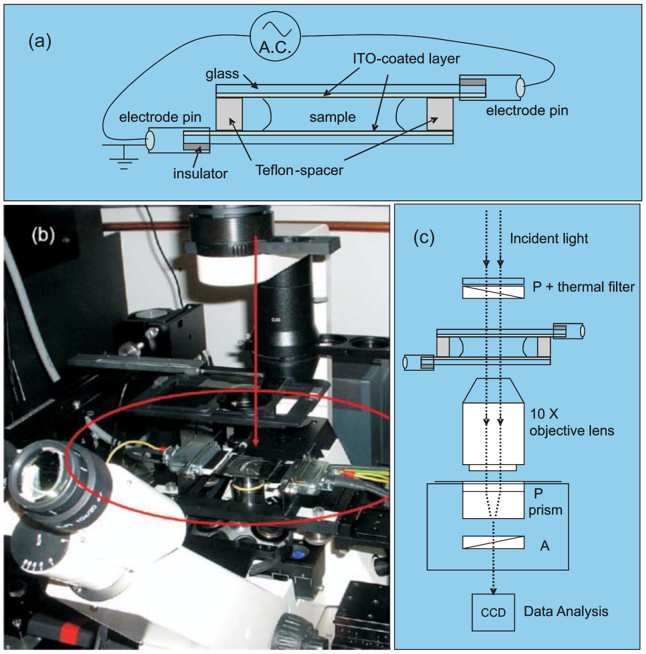

FIG. 2. (Color) (a) A schematic side view of the ITO electric cell, where the sample is loaded between two ITO glass substrates. The electric field is directed normal to the ITO substrates, (b) a real view of the optical microscope with the mounted electric cell, and (c) a schematic of the optics. The direction of the electric field is always along the field-of-view. De-polarized images are recorded in order to probe (local) orientational order. DIC is used to enhance optical contrast (PlasDIC from Carl Zeiss, Axiovert 40CFL). Images are recorded with a CCD camera for data analysis. Here, P indicates a polarizer, A is the analyzer.

performed at the center of the sample to ensure a homogeneous electric field.

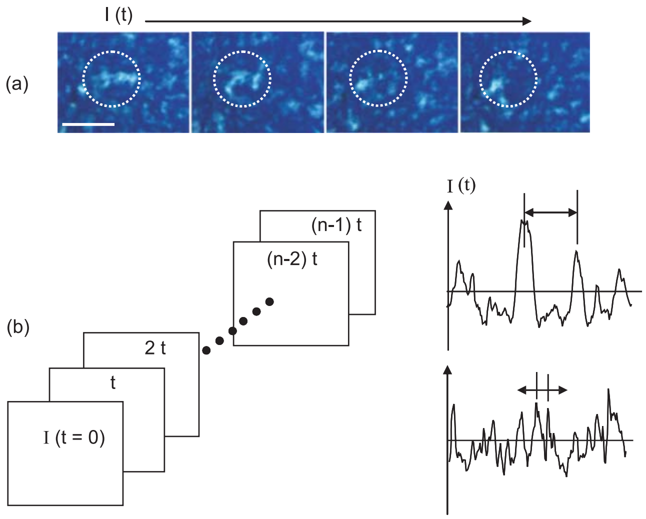

FIG. 3. (Color) The principles of image intensity time-correlation spectroscopy: (a) An example of a few time-lapsed images. The scale bar on the left bottom image corresponds to 200 μm. The white dotted circle indicates a region where marked changes in structure can be seen. (b) A whole series of images shortly after another are recorded to construct image intensity time-correlation functions. The right plots show the measured time variation of the intensity of a single pixel where the dynamics is relatively slow (upper plot with a time step of 1 s, a total measuring time of 100 s, where the correlation-function decay time is 15 s), and fast (lower plot with a time step of 0.3 s, a measuring time of 30 s, where the decay time is 3 s), for a low and high field amplitude, respectively. The time between two peaks, as indicated, is a rough measure for the correlation decay time.

B. Image intensity time-correlation spectroscopy

The *in situ* electric cell is shown with the inverted optical microscope (Carl Zeiss, Axiovert 40CFL model) in Fig. 2(b), together with a schematic of the optics in Fig. 2(c). The direction of the incident light is always along the external electric field, i.e., normal to the two ITO substrates. In order to probe local orientational order, two crossed polarizers are used, together with differential interference contrast (DIC) to enhance the optical contrast in case of inhomogeneous samples (PlasDIC (LD A-Plan 40x) from Carl Zeiss, Axiover 40CFL). Transmitted light images are collected with a CCD camera (AxioCam Color A12-312, 1300 × 1030 pixels). Since the dimensions of morphologies are of the order of tens of microns, we have chosen a low-magnification 10X objective lens (NA 0.30 EC Plan-Neofluar) to probe a relatively large field of view of typically 900 × 700 μm^2. For a time series of images to construct time-correlation functions, we used a field of view of $214 \times 170\,(\text{pixels})^2$, while for the determination of the sizes of nematic domains a field-of-view of $440 \times 310\,(\text{pixels})^2$ is used. The construction and analysis of image intensity time-correlation is done by means of image time-correlation functions, whose definition will be discussed later in this section. We have used AXIOVISION REL. 4.6 software (from Carl Zeiss) for image data acquisition (black/white images up to 16 bit and color images up to 3 by 16 bit).

Image time-correlation functions can be conveniently used for slowly varying structures (slower than, say, 0.1 s) with a linear dimension not less than about 10 μm. This method is useful for any dynamical phenomenon that leads to non-uniform images. We investigated the dynamics of melting and re-forming of nematic domains of charged colloidal rods in an external electric field. The corresponding dynamical state is found at relatively low frequencies and somewhat higher field amplitudes.[9,10] Figure 3(a) shows a few depolarized optical morphologies of small nematic domains that melt and reform, resulting in time-changes of the images, where the white dotted circles mark a region where time-changes are particularly clear.

The dynamics of melting and reforming is quantified through so-called image time-correlation functions as obtained from a time sequence of depolarization-microscopy images with a typical time resolution of $0.3-1$ s. From such a time sequence of images, the image time-correlation function $C_I(t)$ is obtained, which is defined as

$$C_I(t) = \frac{\langle [I(t) - \langle I\rangle(t)]\ [I(0) - \langle I\rangle(0)]\rangle}{\langle [I(0) - \langle I\rangle(0)]^2\rangle}\ . \tag{1}$$

Here, $I(t)$ is the instantaneous transmitted intensity for a given CCD-camera pixel at time t and the brackets $\langle \cdots \rangle$ denote averaging over all pixels. At each time, the pixel-average intensity $\langle I(t)\rangle$ is subtracted from single-pixel intensities $I(t)$ in order to correct for temporal changes of the overall nematic texture. As shown in Refs. 9 and 10, the image intensity time-correlation functions are very accurately represented by a stretched exponential $\exp\{-(t/\tau)^\beta\}$, where β is the stretching exponent and τ is the characteristic time-scale for melting and reforming of the nematic domains. For different types of systems, the time dependence of the image intensity time-correlation function may of course be different. The image-spectroscopy method may be applied, for example, to characterize the relaxation behavior of slow oscillations (the so-called "40 Hz oscillations," which actually vary from 30 to 70 Hz) in neurons, to characterize the stimuli-dependent response in neural networks.[31]

Figure 3(b) shows the principle scheme for the construction of time-correlation functions. On the left, a time sequence of 2D images is depicted. The right figures show intensity traces for a single pixel for two electric field amplitudes. As it can be seen from these traces, the characteristic time of melting and re-forming of nematic domains depends strongly on the field amplitude: the temporal intensity variation in the upper right plot is much slower varying as compared to the lower plot.

In order to construct accurate image intensity time-correlation functions, images must be collected in a time step that is typically ten times smaller (or less) than the decay time of the correlation function. In addition, a minimum number of independent events should be recorded and averaged, which sets the combination of measuring time (relative to the decay time of the correlation function) and the field of view (relative to the area of a single nematic domain). This operational condition will be quantified on the basis of experiments in Sec. III A.

C. Electric birefringence and orientational order

Orientational order in suspensions of rods results in an anisotropic macroscopic refractive index which can be measured, using the sample cell described earlier, by means of a vertically aligned birefringence setup. The optical train of the setup is given in Fig. 4. In case of rod-alignment along the electrical field, the optical train must be rotated as shown in Fig. 4.

A laser beam passes through a Glan-Thompson polarizer, which is oriented at 45° with respect to the direction that is perpendicular to the plane in which the entire optical train can be rotated. Below the horizontally placed electrical sample cell, a $\lambda/4$-platelet is positioned, with one of its optical axis parallel to that of the polarizer. The transmitted intensity is then measured as a function of the angle α of the orientation of a second Glan-Thompson analyzer. We used BSC002 dual channel APT stepper motor controllers (Melles Griot) supported by high speed digital signal processing technology to provide high resolution microstepping (25.600 steps per revolution). Operations are done by the software stepper motor controller (advanced positioning technology by Melles Griot 17BSC002) that controls the 360° motorized rotation stage (NanoRotator, Melles Griot). In this way, the NanoRotator is set with a certain rotational time step (0.28° in a time step). Transmitted light intensities are measured with a Hammamatsu photosensor tube module (H7468-20), during rotation of the NanoRotator onto which the Glan-Thompson analyzer is mounted. The H7468 series photosensor module is incorporated with a photomultiplier tube (PMT) and the analog data from the PMT can be converted into 12-bit digital data for transfer to a personal computer through a RS-232 interface. Thus we can conveniently amplify the accessible photon current by input in the digital interface, depending on the optical response of the system under investigation.

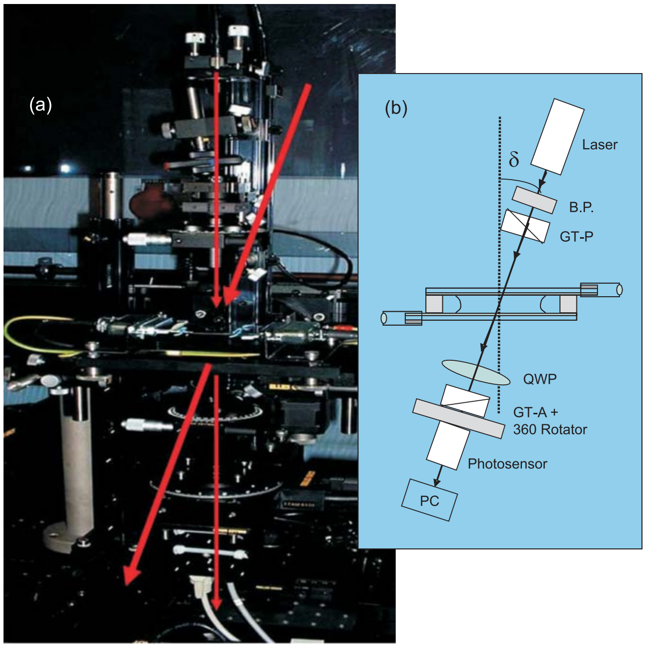

FIG. 4. (Color) (a) A real view and (b) a schematic of the optical elements of the electric birefringence setup: GT-P and GT-A indicate a Glan-Thomson polarizer and analyzer, respectively. The GT-A is mounted on a rotator stage. B.P. is a bandpass filter and QWP is quarter wave plate. The entire optical train can be rotated over a variable angle δ for oblique incidence to the sample in case of rod-orientation along the external field.

For the fd-virus suspensions, where we observed at relatively high frequencies a uniform phase, where the rods are aligned along the direction of the external field (the so-called H-phase).[10,29] In order to measure the orientational order in this homeotropically aligned phase, we have to able to rotate the entire optical train. This is depicted in Fig. 4(b), where the laser beam makes an angle (say δ) with the normal to the flat electrodes of the sample cell. In a measurement, the transmitted intensity is probed as a function of the angle α of the analyzer. The transmitted intensity i varies with the angle α of the analyzer as, $i = (1/2)i_{\max}\,[1 + \sin(2\alpha + \Delta\Phi)]$, where i_{max} is the maximum transmitted intensity and $\Delta\Phi$ is the optical phase shift. From the angle α_{min} where the minimum intensity is measured, the phase shift $\Delta\Phi$ can thus be determined. The angle where the intensity exhibits a minimum (relative to a measurement without the sample) therefore measures the phase shift. Measurements on the field-induced H-phase at normal incidence (with $\delta = 0$) show that there is no birefringence within directions parallel to the electrodes, in accord with the observed uniform intensity distribution under crossed polarizers. Refraction at the water-glass and glass-air interfaces of the sample cell leads to an "apparent birefringence," which increases with increasing angle of incidence δ. The shift of the analyzer angle α_{min} where the minimum in the transmitted intensity occurs due to the cell interfaces has been measured to be less than about 0.2° for δ not larger than about 20°. This is sufficiently small to perform accurate birefringence measurements for $\delta \leq 20°$. From the phase shift $\Delta\Phi$, the difference Δn between the refractive indices along the vertical direction (normal to the electrodes) and the in-plane direction (in-plane with the flat electrodes) can be calculated from

$$\Delta n = \frac{1}{2\pi}\,\frac{1}{\sin^2(\delta)}\,\frac{\lambda}{d}\,\Delta\Phi, \tag{2}$$

where $\lambda = 663\,\mathrm{nm}$ is the laser wavelength in vacuum, $d = d_0/\sqrt{1 - n^{-2}\,\sin^2(\delta)}$ is the optical path length with d_0 being the distance between the two electrodes, and n is the mean refractive index of the suspension. The above formula is valid when Δn is small compared to the mean refractive index. Note that the sign of the measured phase shift $\Delta\phi$ depends on the orientation of the fast axis of the $\lambda/4$-platelet as well as the direction of alignment of the rods. More details on the determination of the direction of alignment of the rods in the H-phase and the interpretation of birefringence measurements can be found in Ref. 10.

The accuracy of the measured refractive index difference Δn is essentially limited by the "apparent birefringence" caused by refraction of the laser beam at the sample-cell interfaces. The absolute error in the measured phase shift $\Delta\Phi$ is less than 0.4° for δ not larger than about 20°. According to Eq. (2) the relative error in Δn is therefore equal to $0.4^\circ/\Delta\Phi[^\circ]$. Since the measured phase shift $\Delta\Phi$ increases proportionally with $\sin^2(\delta)$, in case of homeotropic alignment, the relative error is kept minimal by performing experiments at the maximum angle of $\delta = 20^{\mathrm{o}}$ where the "apparent phase shift" is still limited to within 0.4^{o}.

D. Vertically mounted dynamic light scattering setup

The dynamical light scattering setup is also vertically mounted in order to facilitate the *in situ* electrical cell, as shown in Fig. 5. We used a 35 mW He-Ne laser (JDS Uniphase Model 1145P series, 633 nm wavelength), which is incident perpendicular to the electrical cell and along the external electric field. Two mirrors are used to align the incident laser beam from bottom to top direction. A rotation stage (NanoRotator, Melles Griot) is used as a goniometer, which is controlled by the software stepper motor controller (advanced positioning technology by Melles Griot 17BSC002). To achieve vertical alignment of the incident laser beam, we have used two pinholes and a photon detector on an optical rail. The scattered light is then collected through an optical fiber that is connected to an avalanche photo diode detector. We use an ALV-5000/EPP multiple tau digital real time correlator (by ALV-GmbH, Langen, Germany), which computes photon correlation functions with a linear time-step distribution with time lags between 0.125 μs and 2147 s. The optical fiber is placed on an arm that is connected to the goniometer. An essential element of this vertical DLS is the achromatic lens (with a focal length 75 mm) that is placed on the detection side, to ensure that the scattering volume that is probed is well within the bulk of the sample. Without this lens, in turned out that the measured correlation functions exhibit spurious long-time relaxation. This can be attributed to the scattering of colloids near the electrodes (that is, near the walls of the cell), where hydrodynamic interactions are known to severely slow down their Brownian motion. The electric cell is mounted on a vertical micrometer-ranged translational stage, independently, to optimize the sample height position such that the scattering volume is in between the two electrodes. Both VV- and VH-mode of scattered intensity auto-correlation are possible.

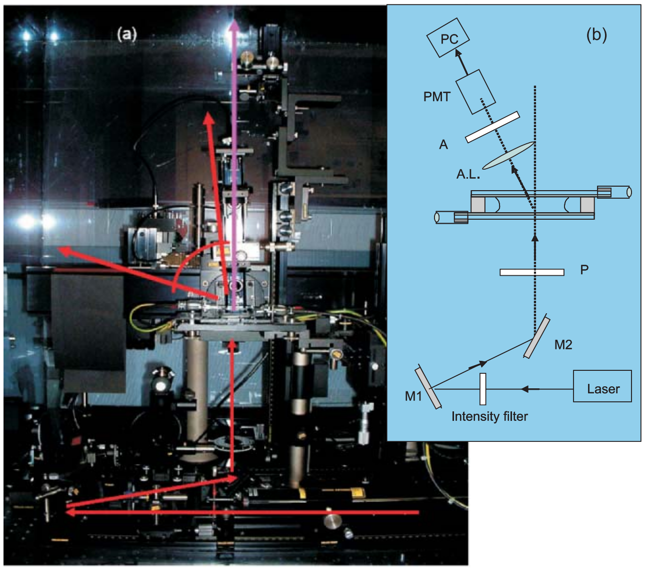

FIG. 5. (Color) (a) A real view and (b) a schematic of the optical elements of the vertical dynamical light scattering setup: P indicates a polarizer, A the analyzer, M1 and M2 are two mirrors, and PMT is a photomultiplier tube. The two mirrors are situated below the sample to be able to align the laser beam in the vertical direction. The achromatic lens (A.L.) between the detector and sample cell is needed to collect scattered intensities only from particles in the bulk of the sample, away from the surface of the electrodes. The sample cell is placed on a micron-ranged translational stage to be able to adjust the sample height to render the scattering volume within the bulk of the sample.

Scattering angles are between 5^{o} and 50^{o}. This setup allows to probe very small scattering angles. Hence, it is possible to perform wave vector dependent measurements where the direction of the wave vector is essentially perpendicular to the electric field direction. The wave vector components parallel and perpendicular to the external field are given by

$$\begin{aligned} q_{\parallel} &= q\ \cos(\Theta_s/2)\ , \\ q_{\perp} &= q\ \sin(\Theta_s/2)\ , \\ q &= \frac{4\pi}{\lambda_n}\ \sin(\Theta_s/2)\ , \end{aligned} \tag{3}$$

where λ_n is the wavelength in the dispersion (of refractive index n) and Θ_s is the true scattering angle. The true scattering angle is calculated from the goniometer angle with Snell's law.[29] The difference between the two angles is insignificant for scattering angles lower than 20^{o}. For such small angles, the wave vector is essentially perpendicular to the external field. Hence, we can probe the microscopic dynamics of colloid displacements perpendicular to the field at smaller scattering angles, while at somewhat larger scattering angles also dynamics parallel to the field can be observed.

Due to scattering of the incident laser beam from optical imperfections at the sample-cell interfaces, there is slight heterodyning, which diminishes the accuracy of measured diffusion coefficients. In order to estimate the accuracy with which diffusion coefficients can be obtained with our setup, we measured the diffusion coefficient of silica spheres as a function of the scattering angle.[10] The scatter in measured diffusion coefficients is about 10%, independent of the scattering angle within the range of 5^{o}–50^{o}. The same system was also probed with a standard DLS apparatus, where the measurement error was found to be about 2%. The reason for the larger experimental error in our setup is due to the above mentioned heterodyning.

III. EXPERIMENTAL RESULTS

With the *in situ* electric instruments for both image correlation spectroscopy and dynamic light scattering, we are able to characterize both slow dynamics of large, mesoscopic structures (tens of microns) and relatively fast microscopic particle dynamics of colloidal systems. Slow dynamics of large structures is exhibited by fd-virus suspensions at low frequencies and relatively large field amplitudes, where a dynamical state is found of melting and reforming nematic domains. Dynamic light scattering is used to probe the collective dynamics in the field-induced uniform phase of homeotropically aligned fd-virus particles (the H-phase). Orientational order in the H-phase is probed with the vertical birefringence setup at off-normal incidence. In the following subsections we present some experimental results to illustrate the performance of the *in situ* electrical instrumentation.

Fd-virus particles have a relatively low scattering strength and birefringence as compared to other, typically inorganic, rod-like colloids. The performance of our setups, as illustrated in the present section for fd-virus suspensions, sets in this sense a lower limit.

A. Mesoscopic characteristic time and microscopic relaxation time

Image correlation functions (see Eq.(1)) are a meaningful tool to characterize the dynamics of melting and forming nematic domains in the field-induced dynamical states as a function of the field amplitude and frequency. Typical dynamic image correlation functions are shown in Fig. 6(a), where the arrow indicates decreasing characteristic times for melting and reforming of nematic domains with increasing field amplitude. The typical size of the domains is 30 μm and the characteristic times for melting and reforming vary from about 1 to 20 s. The solid lines in Fig. 6(a) are fits to the stretched exponential

$$C_I(t) \;=\; \exp\{-(t/\tau)^{\beta}\}\ , \tag{4}$$

where τ defines the characteristic time scale on which nematic domains melt and reform and β is the stretching exponent.

The solid lines in Fig. 6(a) are fits to the stretched exponential form in Eq. (4). As it can be seen, the experimental data are very well described by a stretched exponential. The value of the stretching exponent β is in the range of $0.7-0.8$. There thus seems to be a distribution of relaxation times. This is probably related to the fact that not all nematic domains have the same size and therefore exhibit slightly different melting and forming times.

As it can be seen from Fig. 6(a), the base-lines at large times are not flat, which is due to the finite accuracy of the measured data points. The variation of these data points for the normalized correlation function around zero is a measure for the accuracy per data point, which is thus found to be about 0.02. This accuracy is attained for a measuring time of 100 times the correlation-function decay time and a field of view that contains about 100 melting and forming domains. The accuracy for other measuring times T and number N of domains within the field of view is thus equal to $K\,[\,T\;N\,]^{-1/2}$, where the proportionality constant is equal to $K\,=0.02\times[\,100\,\tau\;\times100\,]^{1/2}=2\times[\,\tau\,]^{1/2}$, where τ is the correlation-function relaxation time (in the same units as T in the former equation). In order to have a proper image of a single domain, the minimum number of pixels (irrespective of their own dimensions) per domain was found to be $10\times10=100$. Since in our measurements we had typically 100 domains within the field of view, this means that about 10^4 pixels is the minimum for a proper image. As far as the time-lapse between images is concerned, it turned out that $1/10$ of the correlation function decay time is a minimum time step.

Above a critical frequency a uniform phase (the so-called H-phase) is induced where the rods are homeotropically aligned, as in a nematic phase, with the director along the external field. The microscopic dynamics within this phase can be probed with the vertically aligned, small angle dynamic light scattering setup. In a dynamic light scattering experiment, the intensity time autocorrelation function $C(t)$ $=\langle I(0)\,I(t)\rangle$ is measured, where the brackets denote ensemble averaging over the positions and orientations of the colloidal particles. Typical normalized intensity autocorrelation functions are shown in Fig. 6(b) for various scattering angles. We have confirmed that the relaxation times are independent of the field amplitude as well as the frequency throughout the H-phase. There is, however, a small region near the lower frequency boundary of the H-phase where pre-transitional nematic domains are present, which results in an apparent faster relaxation.[29]

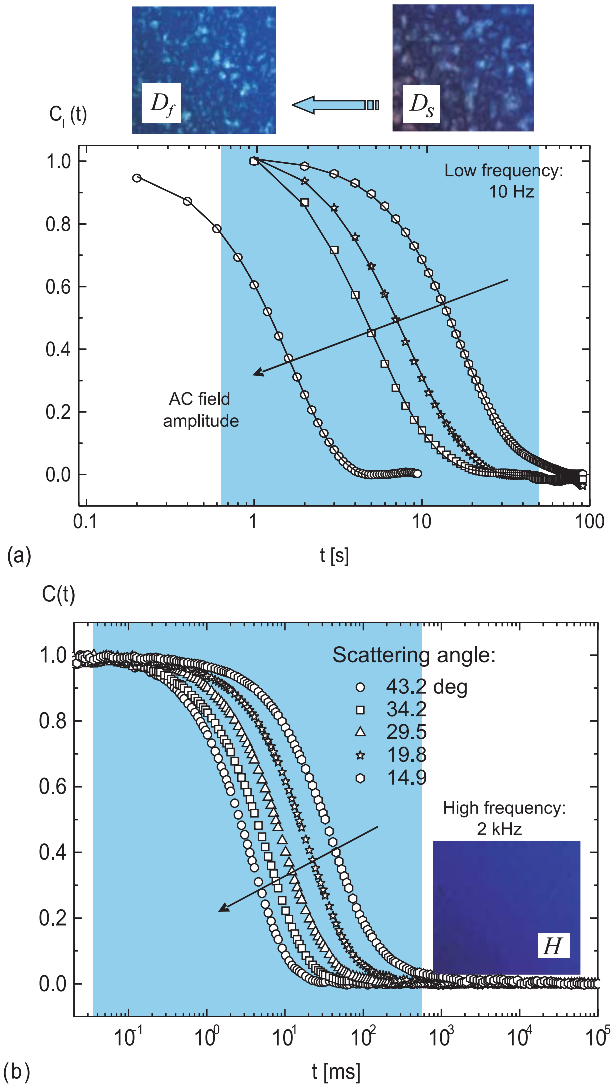

FIG. 6. (Color) (a) Image correlation functions for the dynamical state of melting and reforming nematic domains. The arrow indicates increasing field amplitude and the solid lines are fits to a stretched exponential (typical values of β are in the range $0.7-0.8$). The arrow indicates increasing field amplitude from 3.26, 3.78 , 4.09 V/mm to 5.77 V/mm. (b) Dynamic light scattering correlation functions within the H-phase for various scattering angles as indicated in the figure. Note that the time scales in (a) and (b) are typically three orders of magnitude different: in (a) the relatively slow dynamics of melting and forming of nematic domains is probed, while in (b) diffusion of the fd-virus particles is probed.

Typically, two dynamical modes are found within the H-phase,[32] depending on the scattering wave vector. The scattered-field autocorrelation function $g_E(t)$ can thus be fitted to a sum of two exponentials

$$g_E(t) = A_f \exp\{-(t/\tau_f)\} + A_s \exp\{-(t/\tau_s)^{\beta}\}, \quad (5)$$

where A_f, A_s, τ_f, τ_s, and β are fitting parameters. Here, the subscripts "f" and "s" indicate "fast" and "slow," respectively. According to the Siegert relation, the measured intensity correlation function $C_I(t)$ is proportional to $g_E^2(t)$. According to our scattering geometry,[32] at very small scattering angles, thermal motion of the fd-viruses perpendicular to the electric field is probed, which gives rise to the slow mode. With increasing scattering vectors, above scattering angles of about 20°, in addition to the slow mode, there is a faster dynamical mode with an increasing amplitude that is related to thermal displacements of the rods parallel to the nematic director.[32]

An intriguing field-dependent response is found in an *in situ* electric field DLS measurements, where the photon intensity correlation functions exhibit an oscillatory behavior for relatively large scattering angles. This may be related to electrophoretic motion of the fd-virus particles. The amplitude of these oscillations depends on the external electric field amplitude at low frequency, while the oscillations disappear for relatively high frequencies. Correlation functions exhibiting such oscillations are shown in Fig. 7. These correlation functions are measured at low frequencies, where an inhomogeneous, chiral nematic phase (the so-called N^*-phase) is found, below a frequency of about 500 Hz (for larger frequencies the homogeneous H-phase is entered). This may be related to the electrophoretic motion of the fd viruses along the electric field combined with slight heterodyning (i.e., the scattered intensity from the viruses is mixed with the incident light originating from scattering by optical imperfections at the sample cell interfaces). The frequency of oscillation seems to be independent of the applied field strength (see Figs. 7(a) and 7(b)) and the oscillations disappear at higher frequencies (see Fig. 7(c)).

The oscillatory correlation functions can be fitted with the standard heterodyning form, with a frequency dependent oscillatory velocity of the colloidal rods

$$C(t) = A\, g_E(t) \cos\{q_{\parallel}\, v_0\, t\, \cos(\Omega\, t)\} + C\, g_E^2(t), \quad (6)$$

where $g_E(t)$ is given in Eq. (5). Here, $v_0 \cos(\Omega\, t)$ is the oscillatory electrophoretic velocity and A, v_0, Ω, and C are additional fitting parameters in the fit as compared to the fitting function in Eq. (5). The frequency of the oscillatory motion of the rods is much lower than the applied frequency, which is probably due to the interactions between the rods. Thus one can explore electrophoretic motion at high concentrations in non-equilibrium phases, which would not exist without the external field.

On increasing the field amplitude for the given low frequency of 10 Hz, the amplitude of the oscillations are reduced and less oscillations are found, as shown in Figs. 7(a) and 7(b). For relatively large frequency of the external field, the relaxation time of the correlation function increases dramatically while the oscillations disappear (see Fig. 7(c)). The increasing relaxation time is not yet understood, while the disappearance of the oscillations might be connected to the finite mobility of the interacting rods. That is, the rods are probably too slow to respond to the oscillating field as far as electrophoretic motion is concerned.

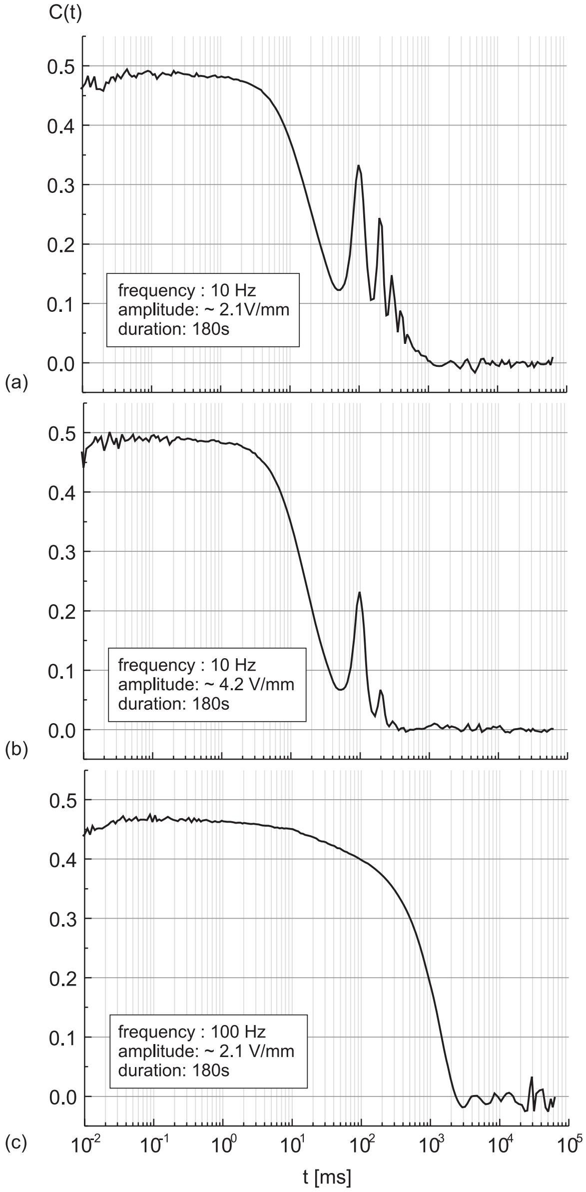

FIG. 7. Examples of field-dependent intensity auto correlation functions that exhibit oscillatory behavior due to electrophoretic motion for a fixed scattering angle (of 25°) and a given fd-concentration and salt concentration: (a) For a low frequency (10 Hz) and low field amplitude (2.1 V/mm). (b) The same as in (a) but now for 4.2 V/mm. (c) The correlation function for a relatively high frequency of 100 Hz.

Typically the scattered intensities from the fd-virus suspensions ranges from 1 to 2 kHz. As mentioned before, this low scattered intensity as compared to other colloidal systems is due to the relatively low scattering strength of the fd-virus particles. Typical measuring times are now relatively large, a few hundreds of seconds, in order to assure an accuracy of data points for the normalized correlation function of about 0.02 as can be seen from the scatter of the points at large times around zero.

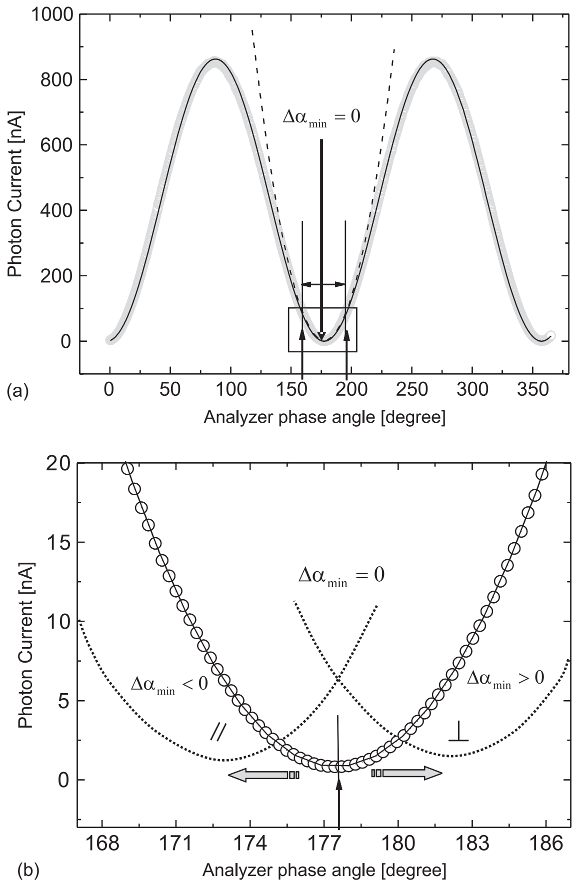

FIG. 8. (a) The transmitted intensity as a function of the analyzer angle α, measured for the sample cell filled with solvent. The grey thick line are data points and the solid line is a fit to the theoretically predicted intensity. The arrows indicate the area where a parabolic fit can be done to accurately determine the location of the minimum. (b) A blow-up of the parabolic fit. The minimum is found at the goniometer off-set angle 177.6 ± 0.2°. The shift of the analyzer angle for a birefringent sample, with fd-virus particles, is positive for perpendicular alignment of the fd viruses and negative for parallel alignment.

B. Field-induced birefringence

An example of a measurement of the transmitted intensity as a function of the analyzer angle is given in Fig. 8. Here, the *in situ* electrical cell is filled with pure buffer without fd-virus. The wide grey line is an accumulation of data points, while the solid line is a fit to the theoretically predicted intensity variation $i = (1/2)i_{\max}\,[1 + \sin(2\alpha + \Phi_0)]$, where i_{max} is the maximum transmitted intensity and Φ_0 is the goniometer off-set angle. An accurate determination of the angle where the minimum occurs is found by fitting a restricted angular range (indicated in Fig. 8(a)) with a parabolic function. Such a fit is presented in Fig. 8(b), which is a larger view of the indicated angular range in Fig. 8(a). The typical accuracy of the angle where the minimum occurs is 0.2°. When for a sample containing a suspension of fd-viruses the phase angle is shifted towards smaller angles (less than the goniometer off-set angle $\Phi_0 = 177.6^{\circ}$), the rods are aligned parallel to the electric field. This depends on the orientation of the fast and slow optical axis of the polarizer and analyzer, which need to be determined independently.

Electric birefringence measurements have been performed well within the H-phase, i.e., far away as well as within the region where transient pre-transitional nematic domains exist. Throughout the H-phase there is essentially no field dependence of the orientational order.[29] This indicates that the H-phase is stabilized by the external field through a significantly different mechanism as compared to the other phases and states. Due to the finite mobility of ions, polarization is less pronounced at frequencies larger than a few kHz. Electrosmosis and the resulting hydrodynamic interactions might therefore be at the origin of the stabilization of the H-phase. This mechanism of hydrodynamic interactions through electro-osmotic flow might be related to the insensitivity of the orientational order as well as the microscopic dynamics on the field amplitude and frequency throughout the H-phase.

IV. CONCLUSIONS AND SUMMARY

We describe *in situ* instrumentation that allows for the characterization of field-induced phases and dynamical states of colloids in external fields. An electrical cell for the study of response to electric fields is described that can be shared by the various setups. The performance of various instruments is illustrated by measurements on charged colloidal rods: suspensions of fd-virus particles. Such systems have been shown to exhibit various phases and dynamical states, depending on the external field amplitude and frequency.

Image-correlation functions are introduced and measured to characterize the dynamics of large scale structures that slowly vary in time. Dynamical states in suspensions of fd-virus particles are observed where nematic domains melt and form. The image-correlation technique, as applied in this work, thus characterizes the dynamics of melting and forming of the nematic domains. The characteristic time constant for melting and forming of the nematic domains can be found from a fit of the correlation functions with a single stretched exponential. The image-correlation method is generally applicable to any process where micron-sized structures change on a time scale of sub-seconds to hours.

A vertically aligned, small angle dynamic light scattering setup is used to probe the dynamics on the colloidal-particle level. Special care must be taken to exclude scattering contributions from colloidal particles close to the electrodes. Due to hydrodynamic interactions with the walls, particles near the electrodes have a very slow dynamics which leads to spurious long-time decay of intensity correlation functions when the scattering volume is not located within the bulk of sample cell. The scattering angle range is 5–50°, where below 20° the component of the scattering wave vector is mainly perpendicular to the external field, so that the dynamics of Brownian motion perpendicular to the external field is probed. However, above a scattering angle of 20°, thermal motion parallel to the field is also probed, which in some cases reveals electrophoretic motion through an oscillating contribution to the correlation function.

Field-induced orientational order in suspensions of colloidal rods is measured by means of a vertically aligned *in situ* electric birefringence setup with an accuracy for the optical phase-shift angle of about 0.4°. Oblique incidence (say, under an angle δ) is necessary to measure the optical anisotropy in case of homeotropic alignment. The measured birefringence is proportional to $\sin^2(\delta)$, so that large angles δ are preferable to increase experimental accuracy. Due to refraction of the incident laser beam at the sample-cell interfaces; however, the maximum angle is $\delta = 20^{\circ}$. For larger angles of incidence, the "apparent birefringence" due to refraction complies with an angular phase-shift of 0.4°.

The electric field instrumentation described here is shown to be quite effective in identifying and characterization of various phases and dynamical states in fd-virus suspensions that are formed due to an external electric field. The microscopic origin for the observed non-equilibrium phase/state behavior, however, is far from understood. The setups discussed in the present paper could also be applied in the study of the response to different types of external fields than electric fields.

ACKNOWLEDGMENTS

The author thanks Professor J. K. G. Dhont for his scientific interest. This work is partially supported by the EU-FP7 Network "Nanodirect" (Contract No. CP-FP-213948-2).

[1] F. Mantegazza, M. Caggioni, M. L. Jimenez, and T. Bellini, Nat. Phys. **1**, 103 (2005).
[2] A. Eremin, R. Stannarius, S. Klein, J. Heuer, and R. M. Richardon, Adv. Funct. Mater. **21**, 556 (2011).
[3] E. Prodan, C. Prodan, and J. H. Miller, Biophys. J. **95**, 4174 (2008).
[4] L. A. Rosen and D. A. Saville, Langmuir **7**, 36 (1991).
[5] P. N. Sen and W. C. Chew, J. Microwave Power Electromagn. Energy **18**, 95 (1983).
[6] M. Mittal, P. P. Lele, E. W. Kaler, and E. M. Furst, J. Chem. Phys. **129**, 064513 (2008).
[7] O. D. Velev, S. Gangwal, and D. N. Petsev, Annu. Rep. Prog. Chem., Sect. C: Phys. Chem. **105**, 213 (2009).
[8] M. Grzelczak, J. Vermant, E. M. Furst, and L. M. Liz-Marzan, ACS Nano. **4**, 3591 (2010).
[9] K. Kang and J. K. G. Dhont, Europhys. Lett. **84**, 14005 (2008).
[10] K. Kang and J. K. G. Dhont, Soft Matter **6**, 273 (2010).
[11] H. Sumi and R. A. Marcus, J. Chem. Phys. **84**, 4894 (1986).
[12] V. Nagarajan, A. M. Brearley, T. J. Kang, and P. F. Barbara, J. Chem. Phys. **86**, 3183 (1987).
[13] M. Maroncelli and G. R. Fleming, J. Chem. Phys. **86**, 6221 (1987).
[14] M. Maroncelli, J. Chem. Phys. **94**, 2084 (1991).
[15] L. Perera and M. L. Berkowitz, J. Chem. Phys. **96**, 3092 (1992).
[16] Y. Gu, A. Widom, and P. M. Champion, J. Chem. Phys. **100**, 2547 (1994).
[17] P. V. Kumar and M. Maroncelli, J. Chem. Phys. **103**, 3038 (1995).
[18] S. Mukamel, *Principles of Nonlinear Optical Spectroscopy* (Oxford University Press, New York, 1995).
[19] W. P. de Boeij, M. S. Pschenichnikov, and D. A. Wiersma, J. Phys. Chem. **100**, 11806 (1996).
[20] H. Chen, Y. Chen, D. Dilworth, E. Leith, J. Lopez, and J. Valdmanis, Opt. Lett. **16**, 487 (1991).
[21] B. B. Das, K. M. Yoo, and R. R. Alfano, Opt. Lett. **18**, 1092 (1993).
[22] K. Oba, P.-C. Sun, Y. T. Mazurenko, and Y. Fainman, Appl. Opt. **38**, 3810 (1999).
[23] R. Mahon, M. D. Duncan, L. L. Tankersley, and J. Reintjes, Appl. Opt. **32**, 7425 (1993).
[24] K. M. Yoo and R. R. Alfano, Opt. Lett. **15**, 320 (1990).
[25] J. Sambrook, E. F. Fritsch, and T. Maniatis, *Molecular Cloning: A Laboratory Manual* (Cold Spring Harbor Laboratory Press, New York, 1989).
[26] K. Zimmermann, H. Hagedorn, C. C. Heuck, M. Hinrichsen, and H. Ludwig, J. Biol. Chem. **261**, 1653 (1986).
[27] K. Kang, A. Wilk, A. Patkowski, and J. K. G. Dhont, J. Chem. Phys. **126**, 214501 (2007).
[28] K. Kang and J. K. G. Dhont, Eur. Phys. J. E **30**, 333 (2009).
[29] K. Kang, New. J. Phys. **12**, 063017 (2010).
[30] K. Kang, J. Biomed. Sci. Eng. **3**, 625 (2010).
[31] D. Wang and D. Terman, Neural Comput. **9**, 805 (1997).
[32] K. Kang, Europhys. Lett. **92**, 18002 (2010).